Synthetic Antiferromagnetic Nanoparticles as Potential Contrast Agents in MRI

Ruben Van Roosbroeck,[†,‡,*] Willem Van Roy,[†] Tim Stakenborg,[†] Jesse Trekker,[†,§] Antoine D'Hollander,[†,§] Tom Dresselaers,[§] Uwe Himmelreich,[§] Jeroen Lammertyn,[‡] and Liesbet Lagae[†,⊥]

[†]IMEC, B-3001 Leuven, Belgium, [‡]Department of Biosystems, Division of Mechatronics, Biostatistics and Sensors, KU Leuven, B-3001 Leuven, Belgium, [§]Department of Imaging and Pathology, Biomedical MRI/Mosaic, KU Leuven, B-3001 Leuven, Belgium, and [⊥]Department of Physics, KU Leuven, B-3001 Leuven, Belgium

ABSTRACT We present the top-down synthesis of a novel type of MRI T_2 contrast agent with great control over size and shape using a colloidal lithography technique. The resulting synthetic antiferromagnetic nanoparticles (SAF-NPs) yield improved relaxivities compared to superparamagnetic iron oxide alternatives (SPIONs). For T_2 weighted imaging, the outer sphere relaxation theory has shown that the sensitivity of a T_2 contrast agent is dependent on the particle size with an optimal size that exceeds the superparamagnetic limit of SPIONs. With the use of the interlayer exchange coupling effect, the SAF-NPs presented here do not suffer from this limit. Adjusting the outer sphere relaxation theory for spherical particles to SAF-NPs, we show both theoretically and experimentally that the SAF-NP size can be optimized to reach the r_2 maximum. With measured r_2 values up to 355 s^{-1} mM^{-1}, our SAF-NPs show better performance than commercial alternatives and are competitive with the state-of-the-art. This performance is confirmed in an *in vitro* MRI study on SKOV3 cells.

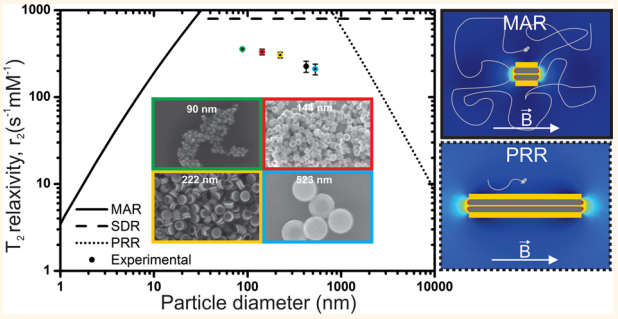

KEYWORDS: magnetic resonance imaging · top-down · synthetic antiferromagnetic nanoparticles · T_2 · contrast agents · relaxation theory

Magnetic nanoparticles show great promise and are widely investigated as agents in various biomedical applications including analyte detection, biosensing, drug delivery and theranostics.[1−3] A particular field of interest is magnetic resonance imaging (MRI) where such particles can serve as contrast enhancers. Most of the reported research related to MRI is focusing on superparamagnetic iron oxide nanoparticles (SPIONs), synthesized by bottom-up wet chemistry methods.[4−6] These particles are very efficient in lowering the transverse (T_2) relaxation time of water proton spins in tissues. This effect is induced by the inhomogeneous magnetic field produced by the SPIONs which results in changes in the Larmor frequency of the precessing proton spins leading to a phase loss in combination with proton diffusion, which prevents refocusing. The efficiency of this process is described by the relaxivity r_2 and is mostly defined as:

$$1/T_{2,\,\text{particles}} = r_2 c_M \qquad (1)$$

and

$$1/T_2 = 1/T_{2,0} + 1/T_{2,\,\text{particles}} \qquad (2)$$

Here, $1/T_{2,0}$ is the relaxation rate in absence of magnetic particles and c_M is the total concentration of magnetic ions. The relaxation rate is thus dependent on the magnetic content of the particle and high r_2 values are desired to increase MRI-sensitivity.

SPIONs are restricted to the superparamagnetic regime to avoid magnetic remanence leading to aggregation in the absence of a magnetic field. This restriction therefore implies a size limit (d = 10−20 nm)[7] and consequently a limited magnetic moment per particle. The ideal particle size for contrast agents in MRI-experiments unfortunately exceeds this limit.[8] To increase the magnetization of SPIONs within the superparamagnetic limit, dopants such as Mn^{2+},[9] Zn^{2+},[10] or other materials such as FeCo[11] have been used. To overcome the size issue, methods for controlled clustering of SPIONs

* Address correspondence to ruben.vanroosbroeck@imec.be.

Received for review October 25, 2013 and accepted February 1, 2014.

Published online February 01, 2014
10.1021/nn406158h

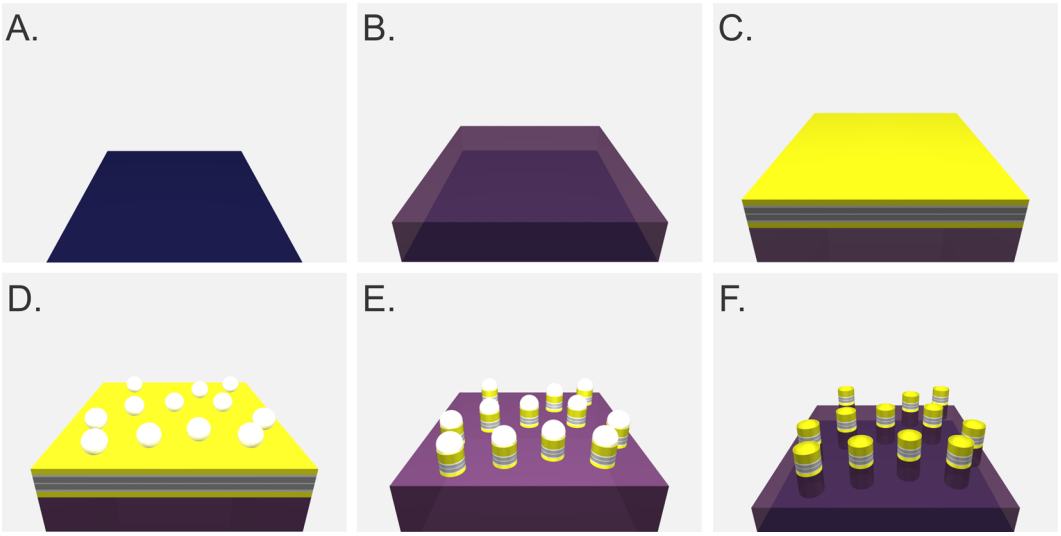

Figure 1. Synthesis process of SAF-NP particles. Starting from a blank wafer (A), resist is spun on the wafer (B) and a magnetic stack is sputtered on top (C). Subsequently, polystyrene beads are drop casted (D), which serve as an etch mask for an ion milling step (E) to create the SAF-NPs. Finally, polystyrene beads are removed using oxygen plasma treatment (F) and the particles are released from the wafer (not shown).

have been designed. This has been done by using hydrophilic or amphipihlic polymers,[12] silane exchange,[13] liposomes,[14] and hydrogels.[15] These approaches unfortunately are tedious and result in clusters of which the size is hard to control.

As an alternative to the above-mentioned limitations we report a new approach for MRI contrast agents, based on synthetic antiferromagnetic nanoparticles (SAF-NPs) that do not suffer from the size limitations SPIONs encounter. When the interlayer exchange coupling effect, also known as RKKY-interaction,[16] is used, highly magnetic SAF-NPs can be synthesized with zero remanence. This effect occurs when two thin layered ferromagnetic alloys such as Fe, Co or Ni are separated by a nonmagnetic spacer layer such as Cr,[17] Ru[18] or Au.[19] Depending on the spacer thickness, ferro- or antiferromagnetic coupling will occur between the ferromagnetic alloys. Here, fine-tuning of the spacer layer thickness resulted in antiferromagneticallly coupled particles that mimic superparamagnetic behavior (*i.e.*, zero remanence) without suffering from the superparamagnetic size limit: due to the antiferromagnetic coupling, the particles show no net magnetic moment in absence of a magnetic field but show a high saturation moment when a field is applied. Furthermore, the fabrication process allows for a very good control of size and shape resulting in monodisperse particle suspensions. As an extra advantage, the controllable synthesis process makes it straightforward to combine magnetic properties with optical or X-ray properties (*e.g.*, through the introduction of gold as a cover), making them ideal candidates for multimodal imaging.

RESULTS AND DISCUSSION

A schematic overview of the standard fabrication procedure of SAF-NPs is shown in Figure 1. With this process, SAF-NPs of various dimensions could be synthesized with high precision and uniformity. Figure 2 shows SEM and HAADF-STEM images of the resulting SAF-NPs. SEM images show that the disk shaped particles are very uniform in size and shape. The layered structure is clearly visible in the HAADF-STEM image in Figure 2E. The particle consists of a [Au(10 nm)/$Ni_{80}Fe_{20}$(5 nm)/Au(2.5 nm)/$Ni_{80}Fe_{20}$(5 nm)/Au(10 nm)] layered structure with a diameter of ≈110 nm. On top of the structure, a crown of redeposited material is visible which is inherent of the ion milling process. The side walls of the particles are covered with a thin redeposited layer as well which can be useful to protect the magnetic layers from the solution in later applications.

Post synthesis, the mean diameter of the resulting SAF-NPs was determined using ImageJ and is shown in Table 1. The SAF-NP diameter ranges from 89.8 to 523.2 nm, which is a 20−30 nm increase compared to the original, nominal bead size. This is due to the slope that is created during the ion milling process. The standard deviation is extremely low for the 143.5, 222.3, and 523.2 nm particles (3−5%) and low for the 89.8 nm particles (20%). The latter shows a larger deviation because of the polydispersity of the original PS-bead solution and the lower precision of the SEM at these dimensions (see Supporting Information). Nevertheless, these measurements show it is possible to synthesize disk shaped SAF-NPs ranging from 89.8 to 523.2 nm in diameter with great precision using colloidal lithography.

After synthesis, the particles were suspended in 2-propanol and coated with 1,2-distearoyl-*sn*-glycero-3-phosphoethanolamine-*N*-[carboxy(polyethylene glycol)-2000]. This amphiphilic phospholipid (PL) consists of a

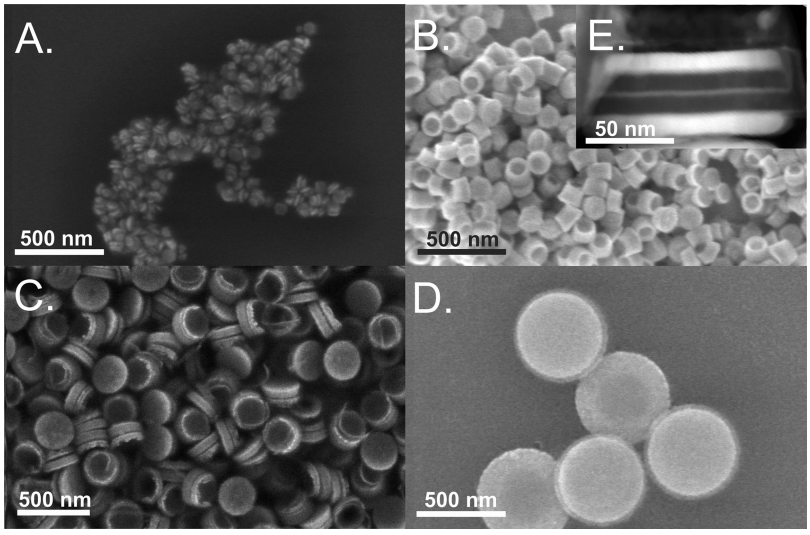

Figure 2. (A–D) SEM-images of SAF-NPs fabricated using (A) 60 nm, (B) 110 nm, (C) 200 nm, and (D) 500 nm polystyrene bead masks. (E) HAADF-STEM-image of a 110 nm diameter SAF-NP. The layered structure of [Au/$Ni_{80}Fe_{20}$/Au/$Ni_{80}Fe_{20}$/Au] is clearly visible. The bright layers on top and bottom are the gold capping layers. The inner magnetic part consists of two $Ni_{80}Fe_{20}$ layers (dark), separated by a gold spacer (bright).

TABLE 1. Mean Nominal Diameter of the PS-Bead Mask, Mean Diameter of the Resulting SAF-NPs (Determined Using SEM) and Their Standard Deviation Determined on at Least 300 Particles, Mean Diameter after Phospholipid Functionalization of SAF-PL-NPs (Determined Using DLS) and the Standard Deviation of 3 Different Measurements, and the Polydispersity Index (PDI, Describes the Width of the Particle Size Distribution) of the DLS Size Distributions of SAF-PL-NPs

PS	SAF-NP	SAF-PL-NP	
nominal (nm)	SEM (nm)	DLS (nm)	PDI
60	89.8 ± 18.6	153.7 ± 2.1	0.14
110	143.5 ± 7.8	205.7 ± 2.8	0.17
200	222.3 ± 9.1	278.2 ± 3.2	0.15
500	523.2 ± 21.1	570.3 ± 4.1	0.19

distearoyl group which provides a hydrophobic tail that can interact with the hydrophobic particle, a phosphate group which creates a negative charge, a long hydrophilic PEG group that can interact with hydrophilic molecules (*e.g.*, water) and a carboxylic end group. This made a phase transfer from organic solvent to water possible thereby creating a stable colloidal suspension with carboxylic groups on the surface of the SAF-NPs, resulting in phospholipid coated SAF-NPs (SAF-PL-NPs).

To determine the hydrodynamic diameter of the SAF-PL-NPs, DLS measurements were performed. This resulted in particles with hydrodynamic diameters of 153.7 ± 2.1, 205.7 ± 2.8, 278.2 ± 3.2, and 570.3 ± 4.1 nm for polystyrene masks of 60, 110, 200, and 500 nm, respectively (Table 1). Compared to the results obtained by SEM, the average diameter increases with 50–60 nm for all particle suspensions. The reason for this size-increase compared to SEM analysis has several origins. First, DLS measurements are performed in suspension leading to a larger hydrodynamic diameter compared to the dry SEM-diameter. Second, the formation of the PEG-phospholipid polymer shell around the particles results in an extra increase of the hydrodynamic diameter of 10–15 nm.[20,21] Further deviations can originate from the disk shape of the particles. Since the DLS system is calculated for spherical particles it determines an equivalent spherical diameter for the SAF-PL-NPs. This is the diameter of a sphere that would give the same DLS signal as the sample under observation.[22] Nevertheless, the DLS size distribution is narrow (see Supporting Information) with polydispersity indices (PDI, describes the width of the particle size distribution) of 0.14–0.19, indicating aggregation is absent in these suspensions. For the smallest particles (60 nm template), a larger standard deviation is observed using SEM, but apparently not in the DLS evaluation. The reason behind this is that DLS is more sensitive toward bigger nanoparticles as they scatter the light more intensely compared to the smaller nanoparticles. As such the smaller nanoparticles are neglected in the specific particle population based on intensity.[23]

To characterize the magnetic properties of the particles, Alternating Gradient Force Magnetometer (AGFM) measurements were performed on the SAF-NPs postsynthesis before release from the carrier wafer. The coupling between the magnetic layers oscillates between ferromagnetic (same direction) and antiferromagnetic (opposite direction) as a function of the spacer layer thickness. Figure 3A shows a similar trend for SAF-NPs, attached to a Si substrate. Results are shown for 222 nm diameter SAF-NPs, consisting of 10 nm $Ni_{80}Fe_{20}$ layers, separated by a Au layer. The saturation field oscillates between ferromagnetic (at 0, 1.5, and 3.0 nm) and antiferromagnetic

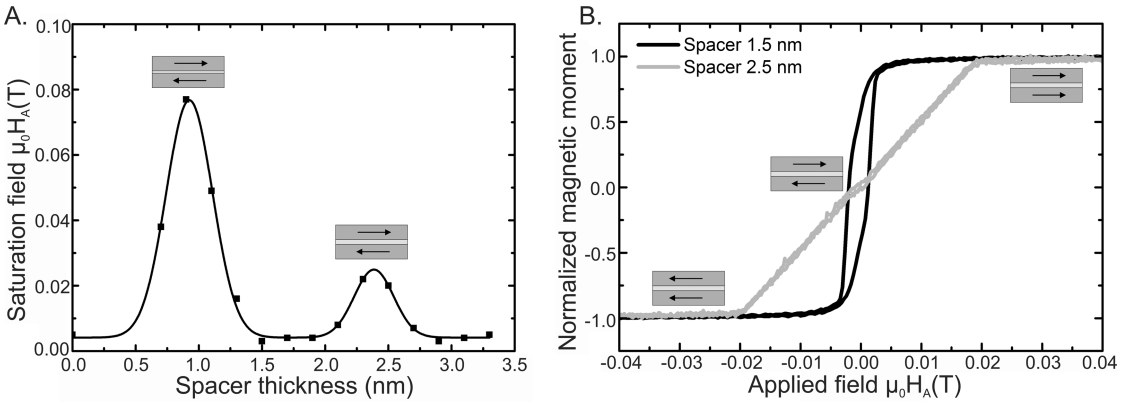

Figure 3. (A) Magnetic saturation field of SAF-NPs in function of the spacer thickness. An oscillation between ferromagnetic (valley) and antiferromagnetic coupling (peaks) can be observed. The trendline is a guide for the eye. (B) Magnetic hysteresis curves of 222 nm SAF-NPs [Au(10 nm)/$Ni_{80}Fe_{20}$(10 nm)/Au(x nm)/$Ni_{80}Fe_{20}$(10 nm)/Au(10 nm)], before release from the carrier wafer. The curves show a clear difference between ferromagnetic coupling (black, x = 1.5 nm) and antiferromagnetic coupling (gray, x = 2.5 nm). The schematic figures represent the magnetization directions of the magnetic layers in antiferromagnetically coupled structures at zero field and saturation field (the gold capping layers are not shown for clarity reasons).

(at 1 and 2.5 nm). Moreover, the oscillation is clearly damped with increasing spacer thickness and the saturation field decreases from 0.08 T at 1 nm to 0.02 T at 2.5 nm. Figure 3B shows the magnetic hysteresis curves for typical antiferromagnetic and ferromagnetic spacer thicknesses at 1.5 and 2.5 nm, respectively. At 1.5 nm, the ferromagnetic coupling results in a high magnetic susceptibility because the two layers tend to align their magnetization spontaneously and can follow the applied field together. Increasing the thickness to 2.5 nm leads to lower magnetic susceptibilities which is typical for antiferromagnetic coupling. These nanoparticles show nearly zero magnetic remanence and coercivity. With increasing applied magnetic field, the moments of the individual ferromagnetic layers scissor toward the field direction until they are in a parallel configuration at the saturation field. Therefore, synthetic antiferromagnetic particles with a spacer thickness of 2.5 nm were further used. After lift-off and functionalization, the saturation magnetization (M_s) in suspension was determined using Superconducting Quantum Ineterference Device (SQUID) magnetometry. An average M_s of 4.15 $\times$ 10^5 A/m (normalized to the magnetic content of the SAF-NPs) was determined which is around 48% of the bulk M_s of permalloy.[24] This M_s value is significantly higher than typical M_s values for SPIONs used in MRI ($(2.7 - 3.7) \times 10^5$ A/m).[25] Because of the possibility to synthesize larger particles using our technique and the higher M_s value compared to SPIONs, the performance of SAF-NPs as contrast agents in MRI was expected to be better. It should be noted that the use of SAF-NPs is not restricted to MRI. For example, it is possible to go to multiplex magnetic separation of biomolecules by tuning the spacer thickness and thus the magnetic susceptibility.[26−30] This way particles can be synthesized that exhibit different magnetophoretic velocities. Due to the combination of antiferromagnetic coupling and

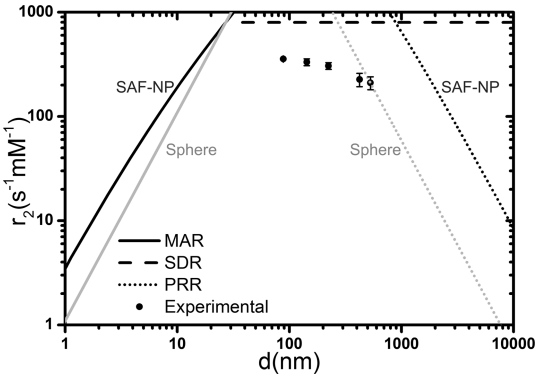

Figure 4. Theoretical (black lines) and measured (points) r_2 values of [Au(10 nm)/$Ni_{80}Fe_{20}$(10 nm)/Au(2.5 nm)/$Ni_{80}Fe_{20}$-(10 nm)/Au(10 nm)] SAF-NPs as function of SAF-NP diameter. The reference theoretical values for spherical $Ni_{80}Fe_{20}$ particles according to Vuong *et al.* are shown in gray. Calculations were performed for a magnetic concentration, c_M = 0.044 mM, a volume fraction, $v = 6.3 \times 10^{-7}$, a saturation magnetization, $M_s = 4.15 \times 10^5$ A/m and an echo time of 12 ms.

their large size, the magnetophoretic velocity of SAF-NPs tends to be much greater than the velocity of superparamagnetic particles which could make them more suitable for various applications including immunomagnetic separation and drug delivery.

To assess the SAF-NP particles for their use in MRI, T_2 relaxivities were measured at 9.4 T and 298 K. The particles were suspended in agar to make sure sedimentation (of the largest particles) had no effect on the measurements. Studies where SPIONS are suspended in agar during relaxivity measurements have already been reported.[31,32] Transverse relaxation rates, R_2 (= $1/T_2$), of different sizes of SAF-NPs were determined and normalized to the magnetic content using the analytical concentration of Ni and Fe, obtained by Inductively Coupled Plasma Optical Emission Spectroscopy (ICP-OES). The thus obtained relaxivities (r_2)

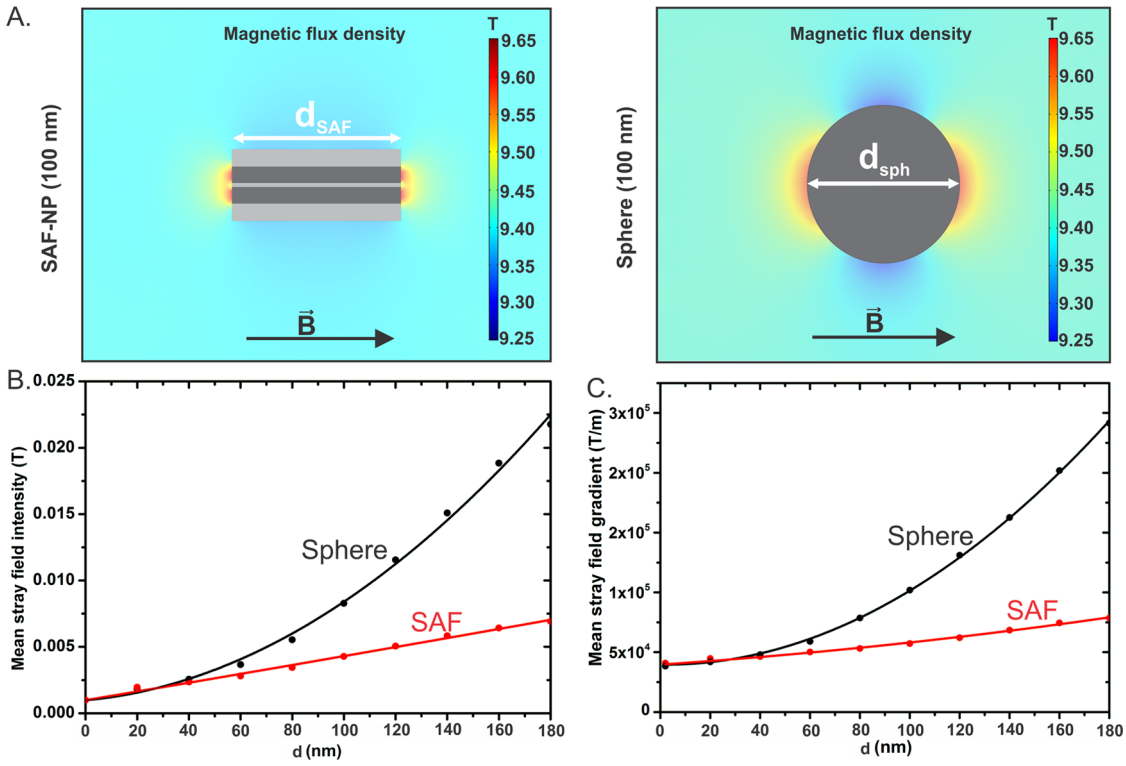

Figure 5. (A) Generated flux density (COMSOL) in the equatorial plane for SAF-NPs (left) and spherical particles (right) with d = 100 nm and M_s = 4.15 × 10^5 A/m under an applied magnetic field, H = 9.4 T. (B) Mean stray field intensity in a 0.6 μm × 0.6 μm × 0.6 μm box as function of the diameter for spherical (black) and SAF (red) particles [Au(10 nm)/$Ni_{80}Fe_{20}$(10 nm)/Au(2.5 nm)/$Ni_{80}Fe_{20}$(10 nm)/Au(10 nm)]. (C) Mean stray field gradient in a 0.6 μm × 0.6 μm × 0.6 μm box as function of the diameter for spherical (black) and SAF (red) particles. The trendlines in (B) and (C) are quadratic fits of the simulation results.

are plotted as a function of the particle diameter (90−523 nm) in Figure 4. From these data, a clear decay is visible with increasing diameter, $d_{SAF\text{-}NP}$. The highest r_2 value is observed for SAF-NPs with a diameter of 90 nm (355 s^{-1} mM^{-1}). The r_2 value then gradually decreases at larger sizes to 331 s^{-1} mM^{-1} at $d_{SAF\text{-}NP}$ = 144 nm, 305 s^{-1} mM^{-1} at 222 nm, 226 s^{-1} mM^{-1} at 422 nm and 210 s^{-1} mM^{-1} at 523 nm. To explain these results, theoretical predictions of the relaxivity are shown in Figure 4 according to the theory of Vuong *et al.*,[8] but adapted to the SAF-NP format as described next.

For spherical particles, the theory describes three relaxivity regimes in the dependence of R_2 on the size of superparamagnetic iron oxide particles. In the motional averaging regime (MAR), R_2 increases with increasing diameter until a maximum is reached at the static dephasing regime (SDR). This is followed by a decrease at even larger diameters in the partial refocusing regime (PRR). In the first regime (MAR), the volume with disturbed magnetic field around the particles is small compared to the proton diffusion length within the echo time. Hence, the protons sample all the different disturbed fields during the echo time. These disturbances are sampled randomly and consequently the dephasing cannot be recovered by a 180° refocusing pulse. In this regime, the transverse relaxation rate (R_2) increases with increasing particle diameter and is described by:

$$R_2 = 1/T_2 = 16/45v\tau_D(\Delta\omega)^2 \qquad (3)$$

where v is the volume fraction of the particles. τ_D = $d^2/4D$ is the translational diffusion time of the protons in the magnetic field inhomogeneities generated by the particles, dependent on the particle diameter d and the translational diffusion constant of water D (2.5 × 10^9 m^2/s at 298 K). $\Delta\omega = \gamma\mu_0 M_s/3$ is the rms angular frequency shift at the particle surface (compared with a point infinitely far away) with γ the gyromagnetic ratio of a proton, μ_0 the magnetic permeability of vacuum and M_s the saturation magnetization of the spherical particles. To convert this model from spheres to SAF-NPs, the average stray field *intensity* generated by spheres with diameter d_{sph} and SAF-NPs with diameter d_{SAF} and thickness t = 42.5 nm [Au(10 nm)/$Ni_{80}Fe_{20}$(10 nm)/Au(2.5 nm)/$Ni_{80}Fe_{20}$-(10 nm)/Au(10 nm)] were calculated using COMSOL (Figure 5), and d_{SAF} was correlated to d_{sph} such that the average stray field intensities are the same. In Figure 5A, the magnetic flux density distribution (H = 9.4 T) of both a spherical particle and SAF-NP with a diameter of 100 nm is depicted. From these simulations it is clear that the induced field inhomogeneity at

this diameter is completely different for both types of particles and thus different behaviors in MRI are expected. Figure 5B shows the simulated mean stray field intensity as a function of the diameter for spherical particles and SAF-NPs. For both types of particles a quadratic relationship between the diameter and the average stray field intensity over the simulated volume could be observed. At very small sizes (d < 30 nm) the induced intensity is larger for SAF-NPs. Because of the fixed magnetic layer thickness (2 × 10 nm), the magnetic content in our SAF-NPs is larger for these sizes compared to spheres. For d > 30 nm the reverse is the case and the mean stray field intensity becomes larger for spheres.

The MAR-regime is valid as long as the particles are small and the protons diffuse fast enough through the particle stray fields (described by the Redfield condition: $\Delta\omega\tau_D < 1$) and R_2 increases with increasing particle diameter d. From the point where d reaches values where the characteristic dimensions of the disturbed field region become larger than the proton diffusion length ($\Delta\omega\tau_D > 1$) not all protons can sense the disturbed field and the dephasing levels off. Without refocusing pulse, and assuming motionless protons, the dephasing only depends on the overall magnetic field distribution and no longer on the proton diffusion length (static dephasing regime). It has been shown for spheres that the relaxation rate is independent of the particle size in this regime. Consequently, the maximum relaxation rate due to (local) field inhomogeneities without refocusing (R_2^*) is constant:

$$R_2^* = \frac{2\pi}{3\sqrt{3}} v\Delta\omega \quad (4)$$

Since simulations of the SAF-NPs did not show conclusive proof that SAF-NPs behave differently from spherical particles in this regime, the same conditions were applied here.

When refocusing pulses are applied, these can partially recover the dephasing, depending on the length scale of the field inhomogeneities and thus the particle size (partial refocusing regime). The smaller the stray field gradient (large particles), the better the recovery and hence the smaller R_2. R_2 then decreases with increasing d and is dependent on the echo time:

$$R_2 = 2.25 \frac{x^{4/3}}{\tau_D} [1.34+vx]^{5/3} \quad (5)$$

with $x = (4/5)^{1/2}\Delta\omega\tau_{CP}$ and τ_{CP} the echo time during the spin−echo sequence (Vuong *et al.*[8]). The longer the echo time, the fewer proton spins are refocused and thus the higher R_2 values reach.

To estimate the relaxation rate in the partial refocusing regime (PRR) for SAF-NPs, the average stray field *gradient* as function of d_{sph} and d_{SAF} was calculated (Figure 4C). Similar to the average field distribution, a quadratic relation could be found between the diameter and the mean stray field gradient for SAF-NPs and spheres. Correlating these relations for the MAR and PRR resulted in apparent spherical diameters $d_{SAF\text{-}NP}$ for which the stray field distribution (MAR) and the stray field gradient (PRR) are matched with the distribution generated by SPIONs of diameter d_{sph}:

$$d_{SAF\text{-}NP} = 2[\alpha(\beta d_{sph}^2/4+\gamma d_{sph}/2+\delta)^{1/2} - \varepsilon] \quad (6)$$

with $\alpha = 1.21 \times 10^7$ (2.88×10^{-1}), $\beta = 3.79 \times 10^{-13}$ (1.78×10^2), $\gamma = 5.56 \times 10^{-12}$ (3.54×10^2), $\delta = 4.08 \times 10^{-9}$ (7.99×10^4) and $\varepsilon = 7.69 \times 10^2$ (8.15×10^2) as empirically defined parameters for the MAR (PRR) regime. This way the relaxation theory of Vuong *et al.* could be converted from spherical particles to SAF-NPs with a good approximation.

Furthermore, the concentration of magnetic ions (c_M) and gold were determined by ICP-OES. Combining these two, the volume fraction (v) could be calculated. The saturation magnetization (M_s) was measured by SQUID. Using these data in eqs 1−6, the three relaxation regimes could be determined as shown in Figure 4. Compared to the original results for spheres, r_2 values for SAF-NPs are higher for small particles (1 nm > $d_{SAF\text{-}NP}$ > 30 nm) because their magnetic content is higher. Consequently, SAF-NPs are theoretically much more potent r_2 contrast agents than SPIONs in this range but in practice, the synthesis of SAF-NPs at these sizes is not possible using colloidal lithography. Above 30 nm, the maximum theoretical r_2^* value of 798 s^{-1} mM^{-1} is reached in the static dephasing regime. This value is only valid in absence of refocusing pulses (r_2^*) but it gives a good approximation of r_2 as long as partial refocusing does not occur with a maximal value at $d_{SAF\text{-}NP}$ = 75 nm ($\Delta\omega\tau_D \approx 10$)[25] after which r_2 decreases slightly again until the PRR is reached. For $d_{SAF\text{-}NP}$ > 30 nm, the volume per particle and the resulting mean flux density gradient for spherical particles increase more rapidly with increasing diameter than for SAF-NPs. As a consequence, the r_2 decay for SAF-NPs in the PRR is less pronounced than for spheres. r_2 values are thus expected to be much higher at large diameters (*e.g.*, 500 nm) than for SPIONs of the same diameters. This way, a broad size range where high relaxivities are observed is introduced using SAF-NPs, making them suitable as T_2 contrast agents at small and large scales.

Comparing our relaxation theory with experimental results, a good qualitative agreement is obtained. The highest experimental r_2 value is observed for SAF-NPs with a diameter of 90 nm (355 s^{-1} mM^{-1}), which is close to the size-optimum predicted by the relaxation theory (75 nm). For larger diameters, a decreasing trend is noticed in the r_2 measurements in accordance to the SDR and PRR. Although the maximum r_2 value is reached around the predicted SAF-NP-size,

the absolute r_2 value differs from the predicted value (355 *vs* 798 s^{-1} mM^{-1}). This discrepancy may have various reasons. In the theoretical predictions we assumed all particles are dispersed separately with an interparticle distance of one micrometer. This is a fair assumption in the absence of a magnetic field, but when a field is applied the particles tend to align in linear chains which results in a reduction of the r_2 rates. The influence of this effect was already investigated theoretically for spherical particles,[3] stating this could lead to relaxivities down to half the value of the corresponding nonaligned spherical particles. Because of their disk shape, this effect could be even more explicit for SAF-NPs and the particles were suspended in agar aiming to avoid or at least minimize this effect. Nevertheless, at the high fields used during the relaxivity measurements, the agar pore size might still have been large enough to allow a partial alignment of SAF-NPs.[33] Alternatively, some particles may already have been clustered prior to suspension in agar. Such clusters would decrease the stray field gradients generated by the particles, contributing to the lowering of r_2 values.

The above relaxivities measured at 9.4 T are also valid in the field range used in clinical scanners. It has been shown theoretically that the main dependence on the applied field of the transverse relaxivity r_2 of magnetic nanoparticles is through the field-dependent magnetic moment of the particles.[34] The moment of our particles saturates at 0.02 T (see Figure 3B), far below the 1.5−3 T used in clinical scanners, and also well below the saturation field of the conventional superparamagnetic contrast agents (≈ 1 T). The fact that r_2 is independent of the field once the particle moment is saturated has also been confirmed experimentally for Endorem particles with r_2 values of 158 s^{-1} mM^{-1} at 1.5 T,[35] 148 s^{-1} mM^{-1} at 7 T, 140 s^{-1} mM^{-1} at 11.7 T and 150 s^{-1} mM^{-1} at 17.6 T.[36] With r_2 values up to 355 s^{-1} mM^{-1}, our SAF-NPs are thus much more effective in reducing T_2 than commercial alternatives like Endorem and competitive with the state-of the art doped (r_2 = 380 s^{-1} mM^{-1})[37] and clustered (r_2 ≈ 400 s^{-1} mM^{-1}) SPIONs. Still, superparamagnetic particles containing Mn[13] or Co[38] show higher relaxivities (r_2 = 528 and 644 s mM^{-1}, respectively) because of their increased saturation magnetization. Similarly, switching to materials like Co or CoFe with higher saturation magnetization than $Ni_{80}Fe_{20}$ can further improve the performance of SAF-NPs as T_2 contrast agents. Moreover, the introduction of a gold capping layer induces a decrease in r_2 performance because this results in the reduced access of protons to the magnetic stray fields of the particle. Since gold is nonmagnetic, it does not influence the stray field distributions. The only relevant parameter is the cap layer thickness. Hence, thicker capping layers result in a worse performance as T_2 contrast agent in MRI and optimization of the capping layer thickness can result in better r_2 performances. Next to gold as capping layer, other materials may be opted for depending on the surface functionalization strategy of choice.

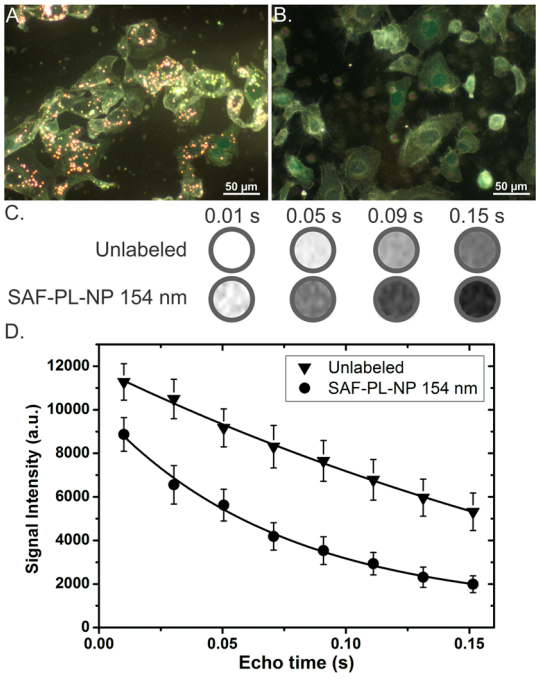

Figure 6. The use of SAF-PL-NPs for MRI using SKOV3 cells as an *in vitro* model. (A) Dark-field microscopic image of SKOV3 cells after overnight incubation with 154 nm SAF-PL-NPs. The interaction of gold coated SAF-PL-NPs (orange) and cells (green) are clearly visible. (B) Dark-field microscopic image of unlabeled SKOV3 cancer cells. (C) MRI images of SKOV3 cells in agar (2500 cells/μL) at different echo times showing an enhanced contrast at all echo times for the 154 nm SAF-PL-NPs (lower) compared to the unlabeled samples (upper). (D) Average T_2 intensity decay (3 samples) in function of the echo time for unlabeled (triangle) and 154 nm SAF-PL-NP labeled (dot) SKOV3 cells. The trendlines are exponential decay fits of the experimental results.

For *in vivo* applications, particle sizes between 10 and 100 nm are typically considered optimal as these are believed to have the longest blood circulation time.[39] However, studies have shown that the rate of clearance for particles with diameters that exceed 100 nm can be reduced by modification of nanoparticle surfaces with coatings that resist reticuloendothelial system interactions, such as polyethylene glycol (PEG).[1] The same work showed long circulations times for PEGylated particles with a hydrodynamic diameter up to 170 nm which could be visualized in tumors by MRI through a period of 24 h. Our best performing 90/154 nm SAF-NPs/SAF-PL-NPs fit well within this range. To demonstrate the feasibility of our fabricated particles for *in vitro* MR imaging, SKOV3-cells were incubated overnight with 154 nm SAF-PL-NPs. After incubation, a clear interaction between the gold coated SAF-PL-NPs and cells was observed using dark field microscopy (Figure 6A). As expected and shown in

Figure 6B, no SAF-PL-NP light scattering was observed for the control cells. With ICP-OES, the $Ni_{80}Fe_{20}$ concentration in labeled cells was determined to be 4.2 pg/cell. To evaluate the MR contrast generation, T_2 weighted images of labeled and unlabeled cells were recorded at 9.4 T in an agar phantom as shown in Figure 6C. The corresponding signal intensities are plotted as function of echo time in Figure 6D. Compared to unlabeled cells, the observed signal intensity decay was more significant for labeled cells. This resulted in a higher contrast generation for any echo time, clearly indicating the effect of the presence of the SAF-PL-NPs and confirming the increased T_2 relaxation for labeled cells. The average of three different cell suspensions was taken to determine the T_2 decay, indicating the reproducibility of the measurements. We thus show that SAF-PL-NPs can be used to efficiently label SKOV3 cancer cells and induce *in vitro* contrast enhancement in T_2 weighted MRI.

Going to clinical use, some structural optimization of SAF-NPs might still be needed. For example, permalloy is not well suited as magnetic material because of nickel toxicity. Although the particles are covered with shielding layers to protect the permalloy layers from the surroundings, it will be hard to exclude *in vivo* toxicity completely. The easy switch to other materials like Co and Mn will therefore prove to be convenient in future clinical studies. Additionally, the imaging capabilities of SAF-NPs do not have to be limited to MRI. The outer particle layers can be engineered because of the layered synthesis approach. By choosing specific materials (*e.g.*, Au), bimodal particles can be fabricated which can be used for combined imaging approaches. As such, SAF-NPs are ideal candidates for multimodal imaging combining their high performance as contrast agents in MRI with other imaging techniques like Computed Tomography (CT), Dark-Field imaging and Photoacoustic imaging.

CONCLUSION

In summary, we were able to fabricate disk shaped, phospholipid coated synthetic antiferromagnetic particles ($Au/Ni_{80}Fe_{20}/Au/Ni_{80}Fe_{20}/Au$) of different sizes ($d$ = 90−523 nm, h = 42.5 nm) with high precision and very small size distributions. Magnetic characterization confirmed the presence of antiferromagnetic coupling between both magnetic layers. This resulted in SAF-NPs that showed a very low magnetic remanence and high magnetization, making them perfectly suited for biomedical applications. In this work, we showed the performance of these SAF-NPs as T_2 contrast agents in MRI. The highest r_2 value of 355 s^{-1} mM^{-1} was observed for the smallest particles with a diameter of 90 nm. As the diameter further increased, the r_2 values dropped. We adapted the theory by Vuong *et al.* from spheres to SAF-NPs by renormalizing the SAF-NP diameter to an equivalent spherical diameter, based on the field and field gradient distributions. Herein, it was demonstrated that our experimental results follow the theory well with an expected maximum at a SAF-NP-diameter of 75 nm in the static dephasing regime followed by a decrease of r_2 for larger diameters in the partial refocusing regime. These results clearly demonstrate the advantage of very uniform, highly magnetic SAF-NPs over SPIONs as the ideal r_2 particle size can be reached, circumventing the superparamagnetic limit. With the use of dark-field imaging, cellular uptake of SAF-PL-NPs in SKOV3 cancer cells was visualized and the labeled cells were detected through MRI, confirming the SAF-PL-NP performance. Their easily controllable synthesis method will make it possible to optimize the SAF-NP structure to induce even better relaxivities in the future.

METHODS

Nanoparticle Synthesis. To synthesize SAF-NPs, a silicon wafer was cleaned by successively submerging in acetone (45 ± 2 °C) and 2-propanol (60 ± 2 °C) for 5 min. Next, a sacrificial photoresist layer (AZ 6612, AZ Electronic Materials) was spun at 5000 rpm for 30 s and baked on a hot plate at 120 °C. With a dc sputter tool, a multilayered stack of [Au(10 nm)/$Ni_{80}Fe_{20}$(10 nm)/Au(2.5 nm)/$Ni_{80}Fe_{20}$(10 nm)/Au(10 nm)] was deposited on top of the sacrificial layer. This was done at a base pressure of 3×10^{-8} mTorr at a rate of 1−3 Å/s. The thickness of each layer was controlled by the deposition time, based on deposition rates that were obtained from X-ray reflectivity (XRR) thickness measurements on separate calibration samples. Polystyrene beads (d = 60, 110, 200, 400, and 500 nm; Sulfate latex, Life Technologies) were applied as a mask by drop casting. First, a positive surface charge was created by immersing the sample in 0.2% (w/v) poly(diallyldimethylammonium) chloride (Sigma-Aldrich) in water for 30 s. After rinsing with water, the PS-beads were drop casted (0.2% (w/v) in water) for 120 s and rinsed again. The SAF-NPs were formed by ion beam etching of the metallic stack in between the PS-beads. Prior to lift-off, organic contaminants were removed by a 10 min O_2-plasma treatment (100 W; 2.3 sccm O_2). Finally, lift-off was performed by dissolving the sacrificial layer in microstrip 2001 (Fujifilm) for 15 min at 85 °C and subsequent sonication for 15 min at 85 °C. After centrifugation (30 min, 5000 rpm), excess microstrip was removed and the suspension was washed in 2-propanol (3×).

Nanoparticle Functionalization. SAF-NPs (200 μg) were washed with chloroform and suspended in 5 mg/mL 1,2-distearoyl-*sn*-glycero-3-phosphoethanolamine-*N*-[carboxy(polyethylene glycol)-2000] (Avanti Polar Lipids) in chloroform (500 μL). After incubation and shaking for 1 h, the sample was dried under nitrogen flow. Finally, the sample was resuspended in water and sonicated to obtain a stable and monodisperse suspension.

Dynamic Light Scattering. The hydrodynamic diameter of the SAF-NPs was measured using a Zetasizer Nano ZS DLS system equipped with a red laser (633 nm) and an avalanche photodiode detector (APD) (Malvern Instruments). Zetasizer software 6.01 was used for analysis. The hydrodynamic sizes reported are based on intensity averages. Along with the hydrodynamic diameter, the polydispersity index (PDI) is given for every sample which describes the width of the particle size distribution. Three distinct measurements were conducted with a fixed detection angle of 173° and the averages and standard deviations of these were calculated and given in Table 1.

SEM/TEM. Prior to SEM imaging, SAF-NPs were dried onto a clean silicon wafer substrate. SEM images were taken using a XL30 FEG instrument (Philips) operated at an accelerating voltage of 5 kV. For TEM analysis, the SAF-NPs were dried onto a carbon-coated copper grid. High-angle annular dark-field scanning transmission electron microscopy (HAADF-STEM) images were taken using a Tecnai F30 ST instrument (FEI) using a FEG electron source at 300 kV.

SEM Size Analysis. To determine the dry SAF-NP size distribution, the diameter of at least 300 particles was measured using ImageJ (NIH) at different spots of the wafer before the lift-off step. The standard deviation of this size distribution was determined on the same amount of particles.

Alternating Gradient Field Magnetometer (AGFM). Measurements were performed on a MicroMag Model 2900 system at a resonance frequency between 400 and 800 Hz. The samples were measured on the wafer, prior to lift-off.

Superconducting Quantum Interference Device (SQUID). The magnetization curves were measured with a commercial superconducting quantum interference device in a field range from $\mu_0 H = -5$ to 5 T. The samples were measured in agar at the same concentration as the original MRI-samples.

Inductively Coupled Plasma Optical Emission Spectrometry (ICP-OES). Prior to ICP-OES measurements, 100 μL of SAF-PL-NPs in water was dissolved in 900 μL of HCl/HNO_3 (20% v/v) and shaken overnight. The samples were diluted with water to an end volume of 5 mL. Reference standards of Au, Ni and Fe (Sigma-Aldrich) were prepared with final concentrations between 0.1 and 10 ppm. The analytical concentration of the samples was determined using an OPTIMA 3300 DV (Perkin-Elmer) tool.

Relaxation Measurements. All T_2 measurements were performed using a 9.4 T NMR-spectrometer (Bruker Biospin). A cpmg sequence was used with a 90° RF-pulse followed by successive 180° pulses to determine r_2 values. Prior to the experiment, SAF-PL-NPs were suspended in a 1% agar solution (Sigma-Aldrich) with an end volume of 800 μL with the desired concentration. Control samples were prepared without SAF-PL-NPs.

COMSOL Simulations. The field distribution of both spherical magnetic nanoparticles (Fe_3O_4) and SAF-NPs [Au(10 nm)/$Ni_{80}Fe_{20}$(10 nm)/Au(2.5 nm)/$Ni_{80}Fe_{20}$(10 nm)/Au(10 nm)] was simulated using the AC/DC module in COMSOL 4.2. Calculations were performed in a 0.6 μm^3 box for multiple particle diameters ($d = 1-200$ nm) under the influence of a homogeneous applied field of 9.4 T.

Cell Culture. SKOV3 cells (ATCCHTB77, Cedex) were cultured in RPMI 1640 medium supplemented with 10% FCS, 50 units/L penicillin, 50 μg/mL streptomycin, and 1×10^{-5} mol L-glutamine. Cells were incubated at 37 °C in a 5% CO_2 environment. All cell culture reagents were obtained from Life Technologies (Ghent, Belgium).

***In Vitro* Cell Preparation.** For uptake confirmation, 500 000 cells per well were seeded in a 6 well plate. SAF-PL-NPs (50 μg in 1 mL) were added after cells attached (typically after 24 h) and incubation continued for 24 h. Next, cells were washed with PBS and again incubated overnight with fresh, SAF-PL-NP free medium. After trypsinization, 100 000 cells were acid-digested in HCl/HNO_3 (20% v/v) and diluted with deionized water to a volume of 10 mL for ICP-OES (OPTIMA 3300 DV, Perkin-Elmer). For *in vitro* MRI, 200 000 cells were suspended in 100 μL of PBS, mixed with 100 μL of agar (end concentration of 1%) and loaded into an agar phantom (1.5%) that was prepared using a previously optimized procedure.[40]

***In Vitro* MRI Measurements of SAF-PL-NP Labeled Cells.** Measurements of the cell containing phantom were performed on a Bruker Biospec 9.4 T small animal MR scanner (Bruker Biospin, horizontal bore, 20 cm). A quadrature radio frequency transmit/receive resonator (inner diameter 7 cm, Bruker Biospin) was used for data acquisition. A cpmg sequence was used with a 90° RF-pulse followed by successive 180° pulses. ImageJ (NIH) was applied for image processing. Signal intensities over time were determined as mean values of a homogeneous section of the cell loaded areas in the agar phantoms.

Conflict of Interest: The authors declare no competing financial interest.

Acknowledgment. The authors would like to acknowledge Prof. V. V. Moshchalkov and Dr. J. Li of the Department of Physics, Solid State Physics and Magnetism, KU Leuven for providing access to SQUID and for the assistance during SQUID measurements. Also thanks to Mrs. B. Vandenbroeck of the Department of Metallurgy and Materials Engineering at the KU Leuven for the assistence during the ICP-OES measurements and Dr. P. Favia and Dr. H. Bender from IMEC for the TEM-imaging.

Supporting Information Available: Dynamic light scattering data, SEM size distribution determinations and TEM layer thickness characterizations. This material is available free of charge *via* the Internet at http://pubs.acs.org.

REFERENCES AND NOTES

1. Cole, A. J.; Yang, V. C.; David, A. E. Cancer Theranostics: The Rise of Targeted Magnetic Nanoparticles. *Trends Biotechnol.* **2011**, *29*, 323–332.
2. Parveen, S.; Misra, R.; Sahoo, S. K. Nanoparticles: A Boon to Drug Delivery, Therapeutics, Diagnostics and Imaging. *Nanomedicine* **2012**, *8*, 147–166.
3. Tran, N.; Webster, T. J. Magnetic Nanoparticles: Biomedical Applications and Challenges. *J. Mater. Chem.* **2010**, *20*, 8760–8767.
4. Laurent, S.; Forge, D.; Port, M.; Roch, A.; Robic, C.; Vander Elst, L.; Muller, R. N. Magnetic Iron Oxide Nanoparticles: Synthesis, Stabilization, Vectorization, Physicochemical Characterizations, and Biological Applications. *Chem. Rev.* **2008**, *108*, 2064–2110.
5. Hilger, I.; Kaiser, W. A. Iron Oxide-Based Nanostructures for MRI and Magnetic Hyperthermia. *Nanomedicine* **2012**, *7*, 1443–1459.
6. Shokrollahi, H. Contrast Agents for MRI. *Mater. Sci. Eng., C* **2013**, *33*, 4485–4497.
7. Lu, A.-H.; Salabas, E. L.; Schüth, F. Magnetic Nanoparticles: Synthesis, Protection, Functionalization, and Application. *Angew. Chem.* **2007**, *46*, 1222–1244.
8. Vuong, Q. L.; Gillis, P.; Gossuin, Y. Monte Carlo Simulation and Theory of Proton NMR Transverse Relaxation Induced by Aggregation of Magnetic Particles Used as MRI Contrast Agents. *J. Magn. Reson.* **2011**, *212*, 139–148.
9. Kueny-Stotz, M.; Garofalo, A.; Felder-Flesch, D. Manganese-Enhanced MRI Contrast Agents: From Small Chelates to Nanosized Hybrids. *Eur. J. Inorg. Chem.* **2012**, *2012*, 1987–2005.
10. Bárcena, C.; Sra, A. K.; Chaubey, G. S.; Khemtong, C.; Liu, J. P.; Gao, J. Zinc Ferrite Nanoparticles as MRI Contrast Agents. *Chem. Commun.* **2008**, *19*, 2224–2226.
11. Lee, S. J.; Cho, J.-H.; Lee, C.; Cho, J.; Kim, Y.-R.; Park, Y.-R. Synthesis of Highly Magnetic Graphite-Encapsulated FeCo Nanoparticles Using a Hydrothermal Process. *Nanotechnology* **2011**, *22*, 375603.
12. Pöselt, E.; Kloust, H.; Tromsdorf, U.; Janschel, M.; Hahn, C.; Maßlo, C.; Weller, H. Relaxivity Optimization of a PEGylated Iron-Oxide-Based Negative Magnetic Resonance Contrast Agent for T_2-Weighted Spin-Echo Imaging. *ACS Nano* **2012**, *6*, 1619–1624.
13. Qi, Y.; Shao, C.; Gu, W.; Li, F.; Deng, Y.; Li, H.; Ye, L. Carboxylic Silane-Exchanged Manganese Ferrite Nanoclusters With High Relaxivity for Magnetic Resonance Imaging. *J. Mater. Chem. B* **2012**, *1*, 1846–1851.
14. Soenen, S. J.; Velde, G. V.; Ketkar-Atre, A.; Himmelreich, U.; De Cuyper, M. Magnetoliposomes as Magnetic Resonance Imaging Contrast Agents. *Wiley Interdiscip. Rev.: Nanomed. Nanobiotechnol.* **2011**, *3*, 197–211.
15. Paquet, C.; de Haan, H. W.; Leek, D. M.; Lin, H.-Y.; Xiang, B.; Tian, G.; Kell, A.; Simard, B. Clusters of Superparamagnetic Iron Oxide Nanoparticles Encapsulated In a Hydrogel: A Particle Architecture Generating a Synergistic Enhancement of the T_2 Relaxation. *ACS Nano* **2011**, *5*, 3104–3112.

16. Bruno, P. Theory of Interlayer Exchange Interactions in Magnetic Multilayers. *J. Phys.: Condens. Matter* **1999**, *11*, 9403.
17. Parkin, S. S. P.; More, N.; Roche, K. P. Oscillations in Exchange Coupling and Magnetoresistance in Metallic Superlattice Structures: Co/Ru, Co/Cr, and Fe/Cr. *Phys. Rev. Lett.* **1990**, *64*, 2304–2308.
18. Mauri, D.; Yosida, K. Spin Engineering: Direct Determination of The Ruderman-Kittel-Kasuya-Yosida Far-Field Range Function in Ruthenium. *Phys. Rev. B* **1991**, *44*, 7131–7134.
19. Unguris, J.; Celotta, R. J.; Pierce, D. T. Oscillatory Exchange Coupling in Fe/Au/Fe(100). *J. Appl. Phys.* **1994**, *75*, 6437–6439.
20. Huang, X.; Bronstein, L. M.; Retrum, J.; Dufort, C.; Tsvetkova, I.; Aniagyei, S.; Stein, B.; Stucky, G.; McKenna, B.; Remmes, N.; *et al.* Self-Assembled Virus-like Particles With Magnetic Cores. *Nano Lett.* **2007**, *7*, 2407–2416.
21. Xu, C.; Sun, S. Monodisperse Magnetic Nanoparticles for Biomedical Applications. *Polym. Int.* **2007**, *56*, 821–826.
22. Bowen, P. Particle Size Distribution Measurement from Millimeters to Nanometers and from Rods to Platelets. *J. Dispersion Sci. Technol.* **2002**, *23*, 631–662.
23. Jans, H.; Liu, X.; Austin, L.; Maes, G.; Huo, Q. Dynamic Light Scattering as a Powerful Tool for Gold Nanoparticle Bioconjugation and Biomolecular Binding Studies. *Anal. Chem.* **2009**, *81*, 9425–9432.
24. Elmen, G. W. Magnetic Alloys of Iron, Nickel, and Cobalt. *Bell Syst. Tech. J.* **1936**, *15*, 113–135.
25. Vuong, Q. L.; Berret, J.-F.; Fresnais, J.; Gossuin, Y.; Sandre, O. A Universal Scaling Law To Predict the Efficiency of Magnetic Nanoparticles as MRI T_2-Contrast Agents. *Adv. Healthcare Mater.* **2012**, *1*, 502–512.
26. Hu, W.; Wilson, R. J.; Koh, A.; Fu, A.; Faranesh, A. Z.; Earhart, C. M.; Osterfeld, S. J.; Han, S.-J.; Xu, L.; Guccione, S.; *et al.* High-Moment Antiferromagnetic Nanoparticles with Tunable Magnetic Properties. *Adv. Mater.* **2008**, *20*, 1479–1483.
27. Fu, A.; Hu, W.; Xu, L.; Wilson, R. J.; Yu, H.; Osterfeld, S. J.; Gambhir, S. S.; Wang, S. X. Protein-Functionalized Synthetic Antiferromagnetic Nanoparticles for Biomolecule Detection and Magnetic Manipulation. *Angew. Chem.* **2009**, *48*, 1620–1624.
28. Koh, A. L.; Hu, W.; Wilson, R. J.; Earhart, C. M.; Wang, S. X.; Sinclair, R. Structural and Magnetic Characterizations of High Moment Synthetic Antiferromagnetic Nanoparticles Fabricated Using Self-Assembled Stamps. *J. Appl. Phys.* **2010**, *107*, 9B522.
29. Joisten, H.; Courcier, T.; Balint, P.; Sabon, P.; Faure-Vincent, J.; Auffret, S.; Dieny, B. Self-Polarization Phenomenon and Control of Dispersion of Synthetic Antiferromagnetic Nanoparticles for Biological Applications. *Appl. Phys. Lett.* **2010**, *97*, 253112.
30. Courcier, T.; Joisten, H.; Sabon, P.; Leulmi, S.; Dietsch, T.; Faure-Vincent, J.; Auffret, S.; Dieny, B. Tumbling Motion Yielding Fast Displacements of Synthetic Antiferromagnetic Nanoparticles for Biological Applications. *Appl. Phys. Lett.* **2011**, *99*, 093107.
31. Zhou, T.; Wu, B.; Xing, D. Bio-Modified Fe_3O_4 Core/Au Shell Nanoparticles for Targeting and Multimodal Imaging of Cancer Cells. *J. Mater. Chem.* **2012**, *22*, 470–477.
32. Narayanan, S.; Sathy, B. N.; Mony, U.; Koyakutty, M.; Nair, S. V.; Menon, D. Biocompatible Magnetite/Gold Nanohybrid Contrast Agents *via* Green Chemistry for MRI and CT Bioimaging. *ACS Appl. Mater. Interfaces* **2012**, *4*, 251–260.
33. Righetti, P. G.; Brost, B. C.W; Snyder, R. S. On the Limiting Pore Size of Hydrophilic Gels. *J. Biochem. Biophys. Methods* **1981**, *4*, 347–363.
34. Gossuin, Y.; Gillis, P.; Hocq, A.; Vuong, Q. L.; Roch, A. Magnetic Resonance Relaxation Properties of Superparamagnetic Particles. *Wiley Interdiscip. Rev.: Nanomed. Nanobiotechnol.* **2009**, *1*, 299–310.
35. Bulte, J. W. M.; Vymazal, J.; Brooks, R. A.; Pierpaoli, C.; Frank, J. A. Frequency Dependence of MR Relaxation Times II. Iron Oxides. *J. Magn. Reson. Imaging* **1993**, *3*, 641–648.
36. Klug, G.; Kampf, T.; Bloemer, S.; Bremicker, J.; Ziener, C. H.; Heymer, A.; Gbureck, U.; Rommel, E.; Nöth, U.; Schenk, W. a.; *et al.* Intracellular and Extracellular T1 and T2 Relaxivities of Magneto-Optical Nanoparticles at Experimental High Fields. *Magn. Reson. Med.* **2010**, *64*, 1607–1615.
37. Liong, M.; Shao, H.; Haun, J. B.; Lee, H.; Weissleder, R. Carboxymethylated Polyvinyl Alcohol Stabilizes Doped Ferrofluids for Biological Applications. *Adv. Mater.* **2010**, *22*, 5168–5172.
38. Seo, W. S.; Lee, J. H.; Sun, X.; Suzuki, Y.; Mann, D.; Liu, Z.; Terashima, M.; Yang, P. C.; McConnell, M. V.; Nishimura, D. G.; *et al.* FeCo/Graphitic-Shell Nanocrystals as Advanced Magnetic-Resonance-Imaging and Near-Infrared Agents. *Nat. Mater.* **2006**, *5*, 971–976.
39. Colombo, M.; Carregal-Romero, S.; Casula, M. F.; Gutiérrez, L.; Morales, M. P.; Böhm, I. B.; Heverhagen, J. T.; Prosperi, D.; Parak, W. J. Biological Applications of Magnetic Nanoparticles. *Chem. Soc. Rev.* **2012**, *41*, 4306–4334.
40. Trekker, J.; Leten, C.; Struys, T.; Lazenka, V. V.; Argibay, B.; Micholt, L.; Lambrichts, I.; Van Roy, W.; Lagae, L.; Himmelreich, U. Sensitive *in Vivo* Cell Detection Using Size-Optimized Superparamagnetic Nanoparticles. *Biomaterials* **2014**, *35*, 1627–1635.